Deep Resources Engineering 3 (2026) 100238

Contents lists available at ScienceDirect

Deep Resources Engineering

journal homepage: www.keaipublishing.com/en/journals/deepre/

Full length article

A micromechanics-based multiscale modeling of heterogeneous rocks with a complex microstructure

Wanqing Shen

Department of Civil Engineering, LaMcube, Polytech Lille, University of Lille, Lille 59000, France

A R T I C L E I N F O

Keywords:
Rock mechanics
Civil engineering
Geomaterial
Constitutive model
Multi-scale modeling
Microstructure

A B S T R A C T

For the micromechanical analysis of heterogeneous materials, this study develops a new macroscopic yield criterion tailored to composites exhibiting a porous matrix-inclusion microstructure. At the mesoscale, mineral grains are distributed within a porous medium, while at the microscale, fine pores are localized inside the matrix. The Drucker–Prager (DP) criterion is employed to capture the tension–compression asymmetry of the solid phase. The proposed macroscopic criterion explicitly incorporates the effects of mesoscale inclusion content, microscale porosity, and pressure sensitivity of the solid phase on the overall mechanical response. Based on this criterion, a multiscale constitutive model is established, incorporating an appropriate plastic hardening law and a macroscopic plastic potential. The model is applied to characterize the macroscopic mechanical behavior of a typical claystone. It enables automatic consideration of mineral compositions and their evolution throughout loading, thanks to its micromechanical foundation. Finally, the model is validated through comparisons with experimental data obtained at various depths, under different component conditions and confining pressures.

1. Introduction

Constitutive modeling serves as an effective approach for characterizing the mechanical behavior of materials. Numerous phenomenological models have been developed for geomaterials based on experimental data, as exemplified by the studies in [1–4]. Many of these models rely on classical strength criteria, including the Mohr–Coulomb [5], DP [6], and Hoek–Brown [7] criteria. Nevertheless, such phenomenological frameworks generally do not account for microstructural details or material composition, particularly in the case of heterogeneous materials.

Micromechanics-based multiscale constitutive modeling offers a promising alternative to address this limitation, enabling a more fundamental understanding of the macro–micro mechanical response of heterogeneous materials. These constitutive models can be easily coupled in the numerical modeling for the structure calculation [8]. For instance, Gurson [9] derived an analytical yield criterion for a hollow sphere with a von Mises-type matrix using limit analysis for porous metallic materials. This model explicitly incorporates the effect of porosity on macroscopic behavior, treating it as a damage parameter. Since then, this foundational model has been extensively extended using various homogenization techniques for different material systems.

In the case of porous geomaterials, the von Mises matrix is unsuitable due to the asymmetric response under tensile and compressive loading. To address this issue, pressure-sensitive matrix behaviors have been introduced, such as a Green-type matrix [10], or a Mises–Schleicher one [11]. Owing to its simple linear form, the DP criterion remains one of the most widely used models for predicting the strength of geomaterials and polymeric materials. By incorporating this local yield criterion along with the influence of voids, macroscopic yield criteria have been established in works such as [12–17]. These micromechanics-based criteria offer substantial improvements over phenomenological models by explicitly integrating microstructural information. What is more, the pore structure or porosity also changes with the environment condition, such as the temperature [18,19]. The critical role of porosity on the mechanical and hydraulic properties of carbonate rock has been investigated [20]. Given that porosity significantly degrades the strength of porous materials, a thorough investigation of its effects is essential for ensuring the stability and safety of engineering applications. Some artificial intelligence technologies have also been adopted in rock mechanics and rock engineering for this purpose, such as the one [21,22].

Besides pore structure, the presence of mineral grains also significantly influences the macroscopic mechanical properties of geomaterials. The key characteristics governing their behavior are porosity and

Peer review under the responsibility of Editorial Board of Deep Resources Engineering.
E-mail address: Wanqing.Shen@polytech-lille.fr.

https://doi.org/10.1016/j.deepre.2026.100238
Received 16 November 2025; Received in revised form 30 December 2025; Accepted 12 January 2026
Available online 20 January 2026

the volume fraction of mineral constituents. A representative example is argillite, which has been extensively studied in feasibility assessments for radioactive waste disposal [23]. A numerical study on the safety of nuclear waste isolation in the claystone under coupled hydro-mechanical-seepage processes has been recently carried out [24]. This rock is considered promising geological barrier materials. As noted in [25], the mesoscale structure of argillite consists of mineral grains such as quartz and calcite, while pores are essentially located within the matrix at the microscopic scale. To account for the role of mineral grains in the overall mechanical response, Abou-Chakra Guéry et al. [26] employed Hill's incremental homogenization approach. In that study, argillite was modeled as a three-phase composite comprising a clay matrix, calcite, and quartz grains. The clay matrix was treated as a homogeneous elastoplastic solid obeying the DP criterion. Macroscopic yield criteria have also been developed [16,27,28]. Notably, these studies did not incorporate the effect of porosity. On the other side, the effects of mineral inclusions and the pore structure on coal failure were numerically simulated based on CT scanning [29].

In this study, a new effective yield criterion and a comprehensive constitutive model are developed for geomaterials characterized by a porous matrix-inclusion microstructure. A two-step homogenization procedure is adopted: the first addresses the effect of microscopic pores within the matrix, and the second incorporates the role of mineral inclusions at the mesoscopic scale. The structure of the paper is outlined as follows: in Section 2, a new explicit form of the macroscopic yield criterion is derived, taking into account the influence of micro-porosity at the microscopic level. This formulation generalizes previous models and recovers the exact solution under pure hydrostatic loading for a porous medium with a DP matrix. Subsequently, in Section 3, a complete multiscale constitutive model is established, incorporating an appropriate plastic hardening law and a macroscopic plastic potential. The proposed model is implemented and applied in Section 4 to represent the macroscopic yield surface and stress–strain behavior of a typical claystone. This model explicitly accounts for microstructural characteristics-such as mineral composition and micro-porosity and their evolution under mechanical loading. Validation is performed by comparing model predictions with experimental data obtained under various confining pressures and at different depths. Concluding remarks are provided in Section 5.

2. Establishment of an effective strength criterion for the studied composite

2.1. Representative volume element

In various engineering contexts, heterogeneous materials are frequently encountered, with mineral grains and pores representing two key constituent phases. A relevant example is argillite, which has been selected in France as a potential host rock for radioactive waste disposal. Its microstructure primarily consists of mineral grains, such as quartz and calcite, embedded within a porous matrix. Typically, the grain sizes are significantly larger than those of the pores, resulting in a clear scale separation. To account for the effects of mesoscale mineral grains and microscale porosity on the macroscopic mechanical response of such composite materials, a representative volume element (RVE) with a porous matrix-inclusion morphology, as depicted in Fig. 1. In order to establish an explicit analytical expression for the effective strength criterion, the mineral grains and pores are generally idealized as spherical in shape and assumed to be randomly distributed throughout the material.

Consider a RVE in Fig. 1 with a total volume V, the volumes of the solid phase, pores, and mineral grains are denoted by V_s, V_f, and V_i, respectively. Based on these definitions and the characteristics of the material microstructure, the microscopic porosity and the mesoscopic volume fraction of mineral grains are defined as follows: $f = \frac{V_f}{V_f+V_s}$ and $\rho = \frac{V_i}{V} = \frac{V_i}{V_f+V_s+V_i}$.

Geomaterials exhibit a strong pressure sensitivity and tension-compression asymmetry, for which the DP criterion has become a popular choice. This leads to the assumption that the solid phase obeys the following local yield criterion:

$$\phi(\sigma) = \sigma_d + T(\sigma_m - h) \leq 0 \quad (1)$$

where $\boldsymbol{\sigma}$ represents the local stress of the solid phase; $\sigma_m = \mathrm{tr}(\sigma)/3$ corresponds to the local mean stress, and $\sigma_d = \sqrt{\boldsymbol{\sigma}' : \boldsymbol{\sigma}'}$ defines the local equivalent stress, in which $\boldsymbol{\sigma}'$ is the deviatoric component of the stress tensor $\boldsymbol{\sigma}$, expressed as $\boldsymbol{\sigma}' = \boldsymbol{\sigma} - \sigma_m\mathbf{1}$, with $\mathbf{1}$ denoting the second-order unit tensor. The local frictional coefficient is given by T, and h indicates its hydrostatic tensile strength. This study aims to investigate, through analysis of the microstructure, how mineral grains, micro-porosity, and solid phase properties affect the macroscopic mechanical response of the studied composite.

2.2. Effective strength criterion

Fig. 1 depicts the microstructure under consideration, for which a two-stage homogenization approach is adopted to establish an analytical yield criterion at the macroscopic level. In the initial homogenization step from the microscale to mesoscale, the effects of both micro-porosity and the pressure-sensitive behavior of the solid phase are incorporated. Subsequently, the influence of mineral meso-grains on the overall mechanical response is accounted for during the second homogenization, which transitions from the mesoscale to the macroscale.

Owing to its concise formulation, the yield criterion proposed in [16] is employed here to represent the homogenized response of the porous medium obtained from the first homogenization stage, as adopted in [30]:

$$F^{mp} = \frac{1+2f/3}{T^2}\tilde{\Sigma}_d^2 + \left(\frac{3f}{2T^2} - 1\right)\tilde{\Sigma}_m^2 + 2(1-f)h\tilde{\Sigma}_m - (1-f)^2h^2 = 0 \quad (2)$$

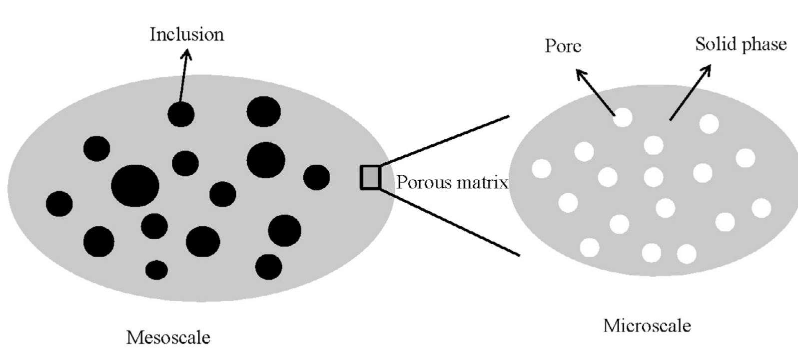

Fig. 1. RVE of the studied composite.

Here, $\tilde{\Sigma}$ serves as the internal stress variable for the porous material at the mesoscale.

The generalized self-consistent method has been applied in [31,32] to study composites reinforced with spherical particles. Novel expressions for the effective bulk modulus κ^{hom} and shear modulus μ^{hom} are presented in Eqs. (A.1) and (A.2), respectively, as detailed in Appendix. For the specific material under consideration, a porous matrix strengthened by rigid particles as depicted in Fig. 1, the corresponding effective bulk modulus κ^{hom} and shear modulus μ^{hom} can be determined using the following formulations:

$$\frac{\mu^{hom}}{\mu^{mp}} = \frac{5\left(\rho^{1/3}-1\right)\left(1-\nu^{mp}\right)\sqrt{U}+K}{R} = S,\ \kappa^{hom} = \frac{3\kappa^{mp}+4\rho\mu^{mp}}{3(1-\rho)}, \text{with}$$
$$\begin{aligned}
R = &-8\left(10\nu^{mp}-7\right)\left(5\nu^{mp}-4\right)\rho^{10/3}\\
&+50\left(8\nu^{mp2}-12\nu^{mp}+7\right)\rho^{7/3}-252\rho^{5/3}\\
&+50\left(8\nu^{mp2}-12\nu^{mp}+7\right)\rho-8\left(10\nu^{mp}-7\right)\left(5\nu^{mp}-4\right)\\
K = &-2\left(5\nu^{mp}-1\right)\left(10\nu^{mp}-7\right)\rho^{10/3}\\
&+50\left(8\nu^{mp2}-12\nu^{mp}+7\right)\rho^{7/3}-252\rho^{5/3}\\
&-75\nu^{mp}\left(\nu^{mp}-3\right)\rho-3\left(15\nu^{mp}-7\right)\left(5\nu^{mp}-4\right)\\
U = &\,36\left(10\nu^{mp}-7\right)^2\left(2\rho^{\frac{17}{3}}+3\rho^{16/3}+5\rho^{14/3}+6\rho^{13/3}+\rho^{6}+4\rho^{5}+7\rho^{4}\right)\\
&+12\left(10\nu^{mp}-7\right)\left(\left(215\nu^{mp}-154\right)\rho^{11/3}\right.\\
&\left.+\left(220\nu^{mp}-161\right)\rho^{10/3}+\left(225\nu^{mp}-168\right)\rho^{3}\right)\\
&+18\left(1300\nu^{mp2}-1890\nu^{mp}+539\right)\rho^{8/3}\\
&+36\left(550\nu^{mp2}-805\nu^{mp}+147\right)\rho^{7/3}\\
&+18\left(900\nu^{mp2}-1330\nu^{mp}+343\right)\rho^{2}\\
&+7\left(5\nu^{mp}-4\right)\left(\left(360\nu^{mp}-252\right)\rho^{5/3}\right.\\
&\left.+\left(275\nu^{mp}-196\right)\rho^{4/3}+\left(190\nu^{mp}-140\right)\rho\right)\\
&+49\left(5\nu^{mp}-4\right)^2\left(3\rho^{2/3}+2\rho^{1/3}+1\right)
\end{aligned} \tag{3}$$

where ν^{mp} is a parameter used in the generalized self-consistent method of [31,32]. For the specific material under consideration in this work, a porous matrix strengthened by mineral grains at the mesoscopic scale, it is a material parameter of the porous matrix.

Following the procedure of modified secant method, one obtains in [30] the effective strength criterion for the studied composite:

$$\begin{aligned}
\boldsymbol{\Phi} = &\frac{\frac{1+2f/3}{T^2}+\frac{2}{3}\rho\left(\frac{3f}{2T^2}-1\right)}{(1-\rho)S}\Sigma_d^2+\left(\frac{3f}{2T^2}-1\right)\Sigma_m^2\\
&+2(1-f)h\Sigma_m-\frac{3+2f+3f\rho}{3+2f}(1-f)^2h^2=0
\end{aligned} \tag{4}$$

in which $\boldsymbol{\Sigma}$ represents the stress of the composite at the macroscale.

However, this yield function should be ameliorated for the effect of porosity. The amelioration of this yield function for the studied composite will be detailed in the following section.

2.3. Amelioration of the yield function Eq. (4)

The mechanical behavior of a porous material under hydrostatic loading will be firstly investigated here, which means that $\Sigma_d = 0$ and $\rho = 0$. Concerning the stress for the porous matrix at the mesoscopic scale, it is defined as $\tilde{\boldsymbol{\Sigma}}$ in the representative volume element as illustrated in Fig. 1. In this special case without the mineral grains at the mesoscale ($\rho = 0$), the corresponding stress is the macroscopic one applied to the exterior of the composite. So, here the symbol $\boldsymbol{\Sigma}$ is adopted for this case. Then, the hydrostatic strength derived from Eq. (4) is expressed as follows:

$$\frac{\Sigma_m}{h} = \frac{(-2T \pm \sqrt{6f})(1-f)T}{3f-2T^2} \tag{5}$$

however, the corresponding exact value for a hollow sphere is given by [13,33,34]:

$$\frac{\Sigma_m}{h} = 1 - f^{\frac{\sqrt{2}T}{(\sqrt{2}T \pm \sqrt{3})}} \tag{6}$$

in which "−" is for the compressive hydrostatic loading, while "+" for the tensile hydrostatic one.

The values of $\frac{\Sigma_m}{h}$ predicted by Eq. (5) is presented as the red surface in Fig. 2, while the exact solution Eq. (6) is the blue surface, as functions of frictional parameter T and porosity f. These two values are nearly identical under tensile loading but diverge significantly in compression.

To enhance the predictive accuracy of the yield criterion Eq. (4) for geomaterials characterized by a porous matrix-inclusion microstructure, specific cases are examined in this study. As previously noted, the current formulation does not adequately account for the influence of porosity f under compressive loading conditions. Therefore, it is pertinent to first investigate the simplified case of a porous material devoid of mineral grains ($\rho = 0$). Leveraging the exact solution for $\frac{\Sigma_m}{h}$ presented in Eq. (6), we aim to refine the macroscopic yield criterion given in Eq. (4).

Starting from the expression of $\frac{\Sigma_m}{h}$ in Eq. (6), the following relation can be derived for a porous material under hydrostatic loading:

$$\underbrace{2f\left(1-\frac{\Sigma_m}{h}\right)\cosh\left[\frac{\sqrt{3}}{\sqrt{2}T}\ln\left(1-\frac{\Sigma_m}{h}\right)\right]}_{M}-f^2-\left(1-\frac{\Sigma_m}{h}\right)^2=0 \tag{7}$$

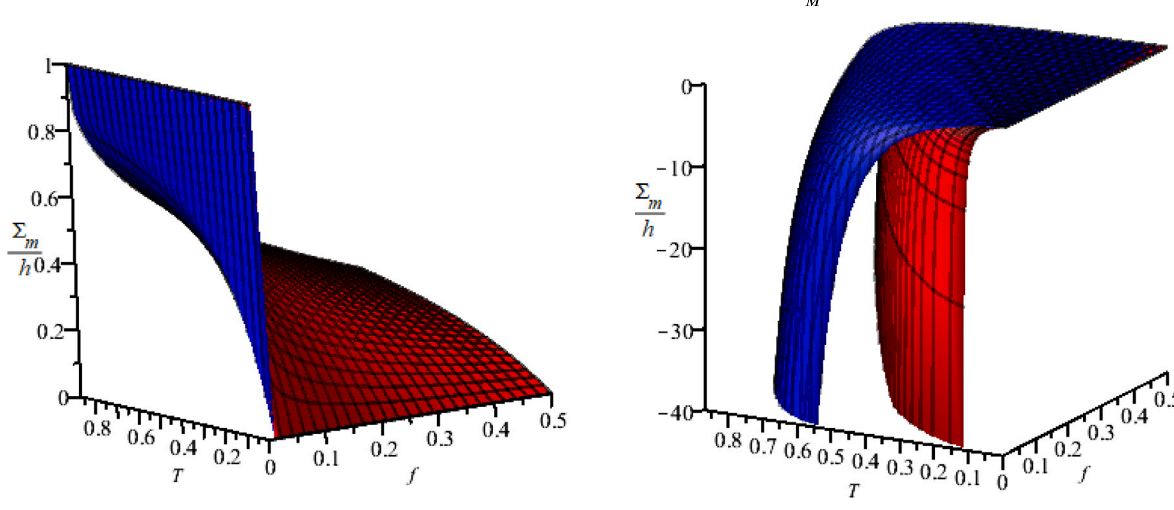

(a) Case of tension (b) Case of compression

Fig. 2. Comparisons between the hydrostatic values of $\frac{\Sigma_m}{h}$ predicted by Eq. (5) (red surface) and the exact solution Eq. (6) (blue surface) as functions of T and f.

What is more, the first term "M" in Eq. (7) can be expanded as follows:

$$\underbrace{2f\left(1-\frac{\Sigma_m}{h}\right)\cosh\left[\frac{\sqrt{3}}{\sqrt{2}T}\ln\left(1-\frac{\Sigma_m}{h}\right)\right]}_{M} = \underbrace{\frac{3f}{2T^2}\frac{\Sigma_m^2}{h^2}+2f\left(1-\frac{\Sigma_m}{h}\right)}_{N}+O\left(\frac{\Sigma_m^4}{h^4}\right) \tag{8}$$

The differences $(M-N)$ between "M" and "N" are illustrated in Fig. 3 as functions of $\frac{\Sigma_m}{h}$ and f with $T=0.8$ for the cases of tension and compression, respectively. The influence of the higher-order terms is obvious. With the increase of f and the absolute values of $\frac{\Sigma_m}{h}$, the difference increases.

Based on these observations, the yield criterion Eq. (4) can be rearranged as follows:

$$\frac{\frac{1+2f/3}{T^2}+\frac{2}{3}\rho\left(\frac{3f}{2T^2}-1\right)}{(1-\rho)S}\frac{\Sigma_d^2}{h^2}+\underbrace{\frac{3f}{2T^2}\frac{\Sigma_m^2}{h^2}+2f\left(1-\frac{\Sigma_m}{h}\right)}_{N} - f^2-\left(1-\frac{\Sigma_m}{h}\right)^2-\frac{3f\rho}{3+2f}(1-f)^2=0 \tag{9}$$

This expression can be simplified as following with the conditions $\frac{\Sigma_d^2}{h^2}=0$ and $\rho=0$:

$$\underbrace{\frac{3f}{2T^2}\frac{\Sigma_m^2}{h^2}+2f\left(1-\frac{\Sigma_m}{h}\right)}_{N}-f^2-\left(1-\frac{\Sigma_m}{h}\right)^2=0 \tag{10}$$

Comparing the expressions of Eqs. (7) and (10), and taking into account the relationship given in Eq. (8), the term N in the criterion Eq. (9) will be replaced by the one M to account for the omitted the higher order term $O(\frac{\Sigma_m^4}{h^4})$. Consequently, one derives the searched effective strength criterion for the studied composite with a complex microstructure:

$$\Phi=\frac{\frac{1+2f/3}{T^2}+\frac{2}{3}\rho\left(\frac{3f}{2T^2}-1\right)}{(1-\rho)S}\frac{\Sigma_d^2}{h^2}+2f\left(1-\frac{\Sigma_m}{h}\right)\times\cosh\left[\frac{\sqrt{3}}{\sqrt{2}T}\ln\left(1-\frac{\Sigma_m}{h}\right)\right]-\left(1-\frac{\Sigma_m}{h}\right)^2-f^2-\frac{3f\rho}{3+2f}(1-f)^2=0 \tag{11}$$

The exact values Eq. (6) can be retrieved automatically by this yield criterion, and it ameliorates fundamentally the one Eq. (2).

3. Development of a multiscale constitutive model based on Eq. (11)

Based on the newly proposed effective strength criterion Eq. (11), which explicitly incorporates the effects of micro-porosity f and meso-inclusion content ρ, a comprehensive multiscale constitutive model will be developed in this section. By integrating the macroscopic plastic potential for the plastic flow rule, plastic hardening, as well as the evolution of f and ρ, the proposed model aims to characterize the effective mechanical response of the studied geomaterials.

3.1. Elastic case

The elastic mechanical behavior of the composite under investigation is governed by its microstructure and its evolution. To incorporate the effects of micro-porosity, solid phase properties, and meso-inclusion content, a two-step upscaling approach will be employed. In light of the specific microstructure examined, the first upscaling step addresses the role of micro-porosity f and the bulk and shear moduli (κ, μ) of the solid phase at the microscale. Using the Mori–Tanaka homogenization scheme [36], the homogenized bulk modulus κ^{mp} and shear modulus μ^{mp} of the porous matrix are derived as follows:

$$\kappa^{mp}=\frac{4(1-f)\kappa\mu}{4\mu+3f\kappa};\quad \mu^{mp}=\frac{(1-f)\mu}{1+6f\dfrac{\kappa+2\mu}{9\kappa+8\mu}} \tag{12}$$

The second upscaling stage incorporates the influence of large mineral grains on the macroscopic elastic properties (κ^{hom}, μ^{hom}). The resulting homogenized bulk and shear moduli are expressed by Eqs. (A.1) and (A.2), respectively, which utilize the previously derived homogenized results for the porous matrix from Eq. (12).

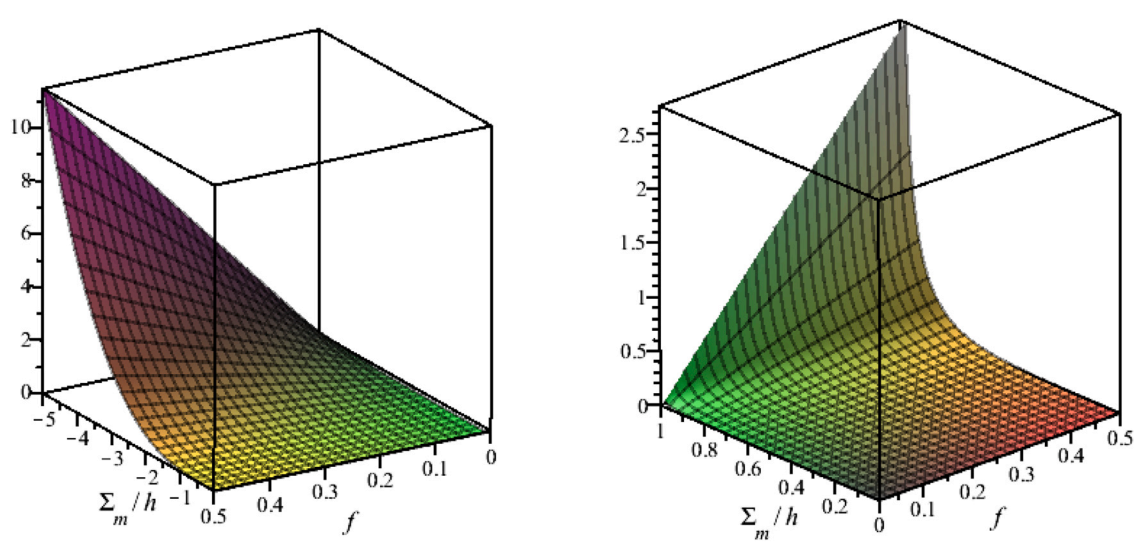

(a) Case of compression (b) Case of tension

Fig. 3. The difference between "M" and "N" given in Eq. (8) as functions of $\frac{\Sigma_m}{h}$ and f, $T=0.8$.

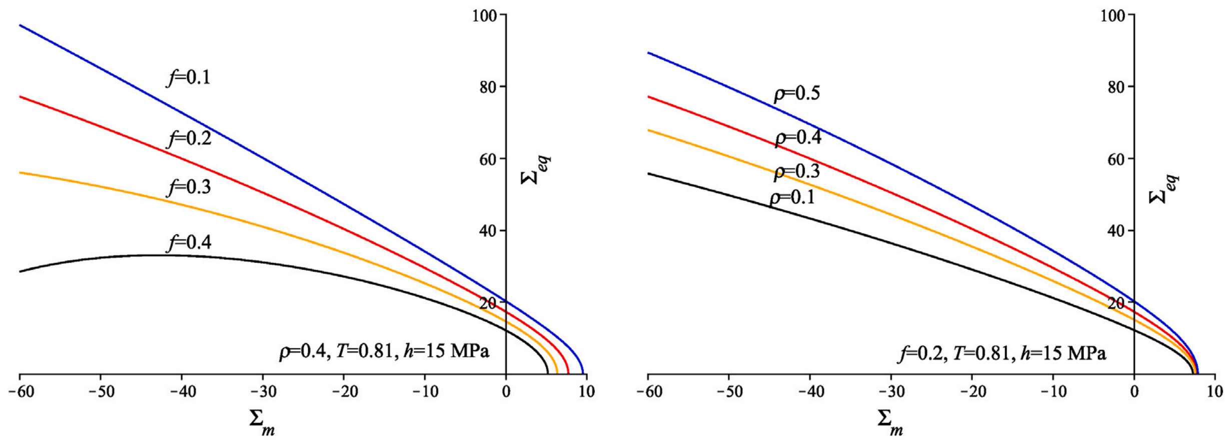

(a) Effect of f (b) Effect of ρ

Fig. 4. The effects of f and ρ on the yield strength of the studied composite, T = 0.81 and h = 15 MPa.

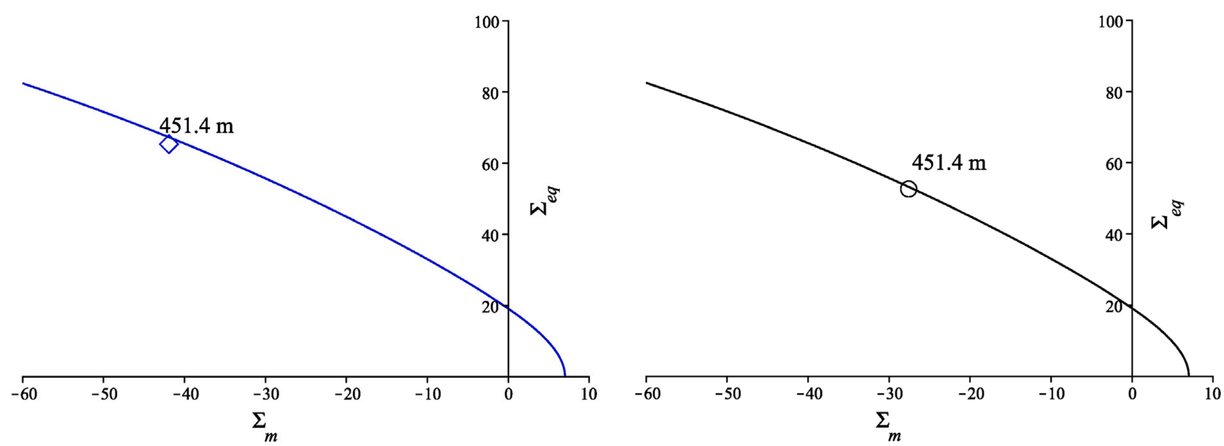

(a) ρ = 49%, f = 23.7%, 0 MPa (b) ρ = 51%, f = 23.6%, 5 MPa

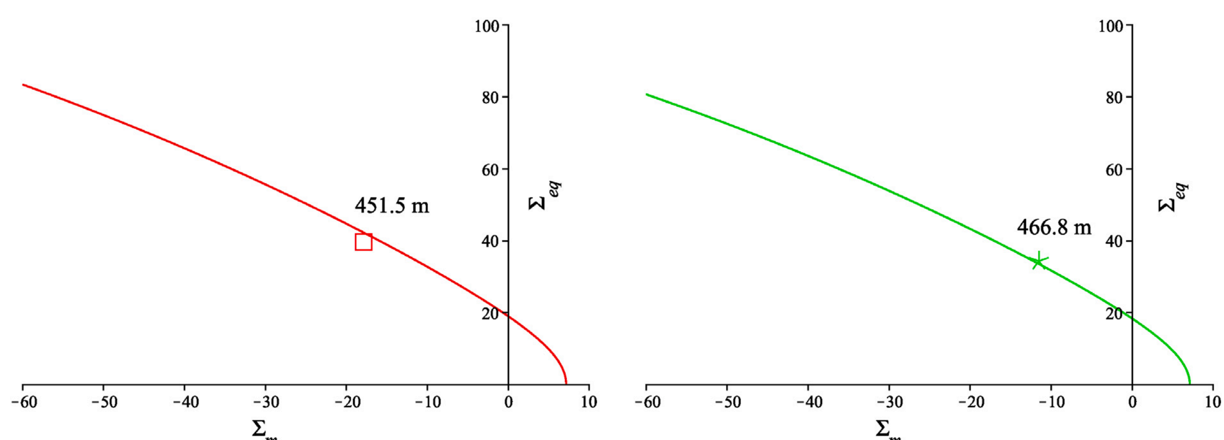

(c) ρ = 53%, f = 25%, 10 MPa (d) ρ = 53%, f = 25%, 20 MPa

Fig. 5. Yield surfaces predicted by Eq. (14) (solid lines) are compared against the experimental data (points) from [35] under various confining pressures: green line (asterisk) - 466.8 m; red line (box) - 451.5 m; black line (circle) - 451.4 m; blue line (diamond) - 451.4 m.

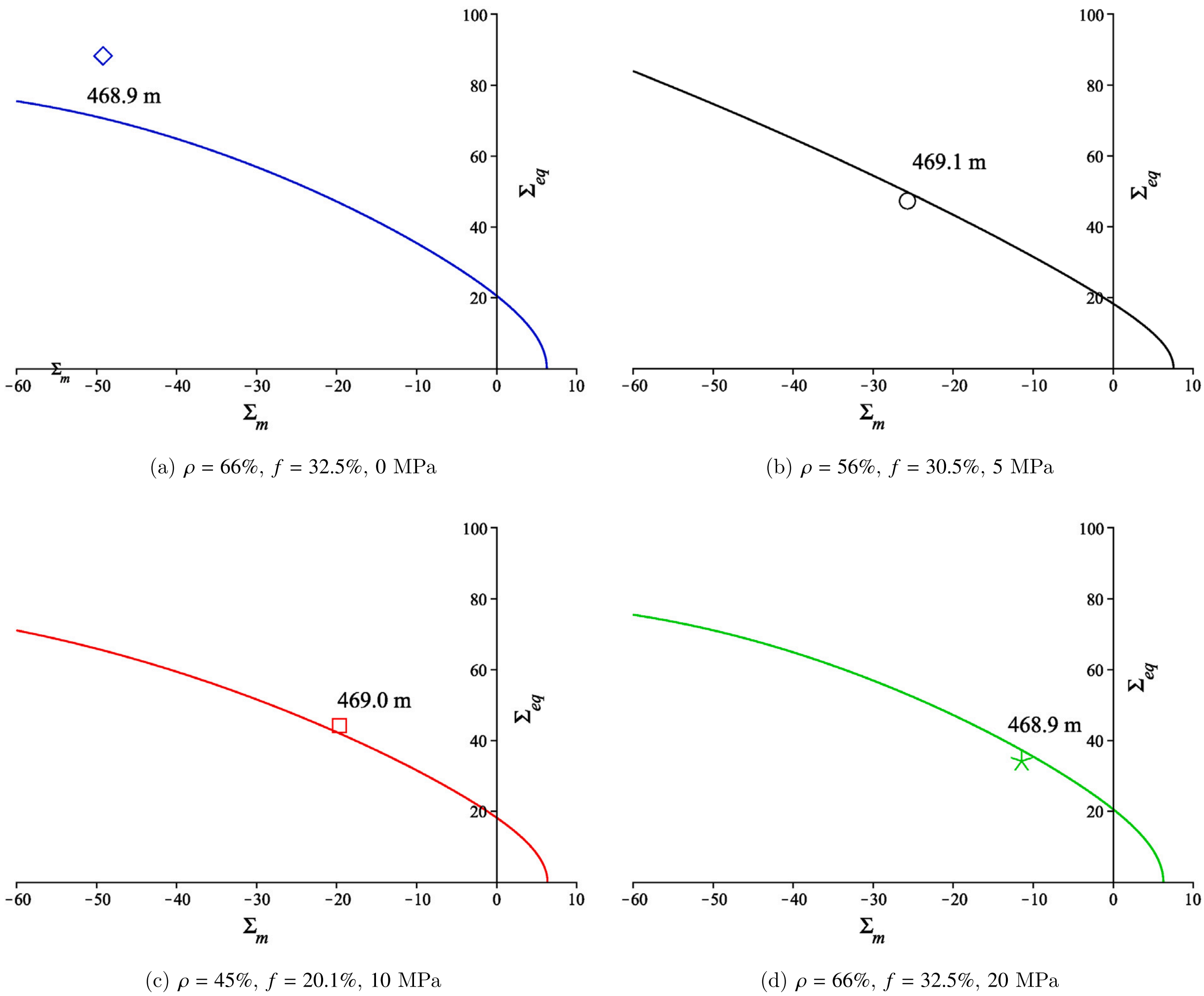

(a) ρ = 66%, f = 32.5%, 0 MPa

(b) ρ = 56%, f = 30.5%, 5 MPa

(c) ρ = 45%, f = 20.1%, 10 MPa

(d) ρ = 66%, f = 32.5%, 20 MPa

Fig. 6. Yield surfaces predicted by Eq. (14) (solid lines) are compared against the experimental data (points) from [35] under various confining pressures: green line (asterisk) - 468.9 m; red line (box) - 469.0 m; black line (circle) - 469.1 m; blue line (diamond) - 468.9 m.

3.2. Plastic case

The plastic response of the composite under investigation is characterized by the newly proposed effective strength criterion given in Eq. (11). In geomaterials, experimental observations often reveal a hardening behavior resulting from accumulated plastic deformations under loading. Following the approach of [37], the plastic hardening of the solid phase is incorporated through the evolution of the frictional coefficient T, which depends on the equivalent plastic strain d^p. Let T_0 represent the initial frictional threshold and T_m its asymptotic value. An exponential hardening law is adopted, expressed as:

$$\bar{T} = T_0 + (T_m - T_0)\frac{d^p}{b_1 + d^p} \tag{13}$$

The rate of plastic hardening is characterized by the parameter b_1.

Consequently, the effective strength criterion can be reformulated as:

$$\begin{aligned}\Phi = {} & \frac{\frac{1+2f/3}{\bar{T}^2} + \frac{2}{3}\rho\left(\frac{3f}{2\bar{T}^2} - 1\right)}{(1-\rho)S}\frac{\Sigma_d^2}{h^2} + 2f\left(1 - \frac{\Sigma_m}{h}\right) \\ & \times \cosh\left[\frac{\sqrt{3}}{\sqrt{2\bar{T}^2}}\ln\left(1 - \frac{\Sigma_m}{h}\right)\right] - \left(1 - \frac{\Sigma_m}{h}\right)^2 - f^2 - \frac{3f\rho}{3+2f}(1-f)^2 = 0\end{aligned} \tag{14}$$

To account for the non-associated flow characteristics inherent to geomaterials, a macroscopic plastic potential is developed herein. The formulation, inspired by [16,38], is presented below:

$$\begin{aligned}\Psi = {} & \frac{\frac{1+2f/3}{\bar{T}\bar{t}} + \frac{2}{3}\rho\left(\frac{3f}{2\bar{T}\bar{t}} - 1\right)}{(1-\rho)S}\frac{\Sigma_d^2}{h^2} + 2f\left(1 - \frac{\Sigma_m}{h}\right) \\ & \times \cosh\left[\frac{\sqrt{3}}{\sqrt{2\bar{T}\bar{t}}}\ln\left(1 - \frac{\Sigma_m}{h}\right)\right] - \left(1 - \frac{\Sigma_m}{h}\right)^2\end{aligned} \tag{15}$$

wherein $\bar{t}$ denotes the dilatancy coefficient governing the transition from volumetric compaction to dilatancy. Since the rate of volumetric dilatancy typically evolves with the history of plastic deformation, $\bar{t}$ here is defined by:

$$\bar{t} = t_0 + (t_m - t_0)\frac{d^p}{b_2 + d^p} \tag{16}$$

in which t_0 represents its initial value and t_m the asymptotic one with $t_m \leq T_m$.

Then, the macroscopic plastic deformation $\boldsymbol{E}^p$ is calculated as follows:

$$\boldsymbol{E}^p = \dot{\Lambda}\frac{\partial \Psi}{\partial \boldsymbol{\Sigma}}(\boldsymbol{\Sigma}, f, \rho, \bar{T}, \bar{t}) \tag{17}$$

in which $\dot{\Lambda}$ is the plastic multiplier.

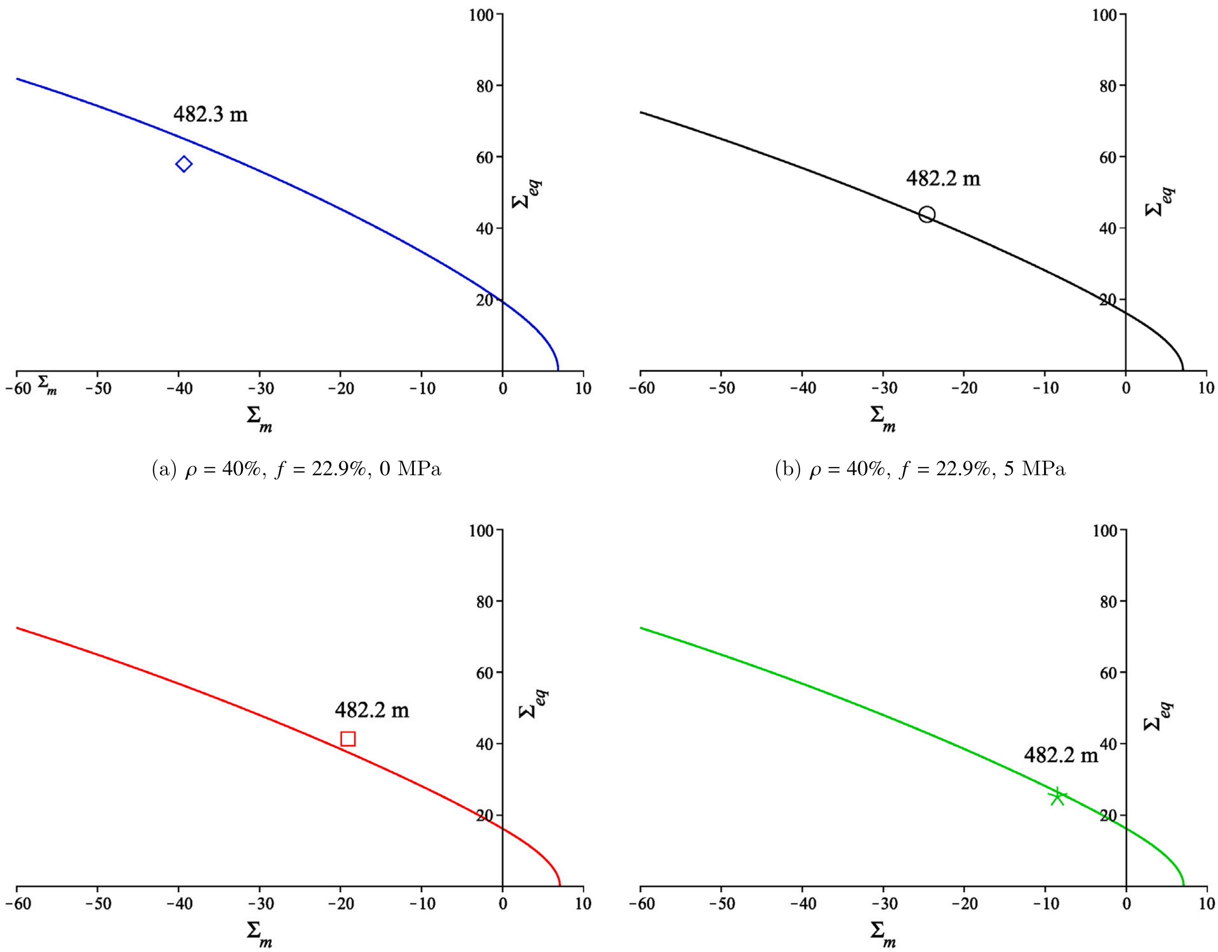

(a) ρ = 40%, f = 22.9%, 0 MPa (b) ρ = 40%, f = 22.9%, 5 MPa

(c) ρ = 40%, f = 22.9%, 10 MPa (d) ρ = 55%, f = 26.2%, 20 MPa

Fig. 7. Yield surfaces predicted by Eq. (14) (solid lines) are compared against the experimental data (points) from [35] under various confining pressures: green line (asterisk) - 482.2 m; red line (box) - 482.2 m; black line (circle) - 482.2 m; blue line (diamond) - 482.3 m.

Following the energy condition proposed by Gurson [9], the equivalent plastic strain rate of the solid phase is given by:

$$\dot{d}^p = \frac{\boldsymbol{\Sigma} : \boldsymbol{E}^p}{(1-f)(1-\rho)\left[\bar{T}h + (\bar{t} - \bar{T})\frac{\Sigma_m}{1-f}\right]} \tag{18}$$

The evolutions of f and ρ are governed by the kinematical compatibility condition, as expressed below:

$$\dot{f} = \frac{1-f}{1-\rho}\mathrm{tr}\mathbf{E}^p - (1-f)\bar{t}\dot{d}^p, \quad \dot{\rho} = -\rho\mathrm{tr}\mathbf{E}^p \tag{19}$$

By employing a user subroutine, the complete constitutive model described previously was integrated into the Abaqus finite element environment.

4. Application to a claystone

A series of experimental investigations have been systematically performed in [25,35,39] to characterize the heterogeneous claystone. The mineral composition of this claystone varies with depth. To analyze how these compositional differences influence its mechanical behavior, triaxial compression tests under various confining pressures (0, 5, 10 and 20 MPa) were carried out on specimens extracted from three distinct depths [35]. These samples thus reflect different material compositions. The primary mineral constituents of the claystone include clay matrix, calcite, and quartz. Porosity is predominantly associated with the clay matrix. The Young's modulus and the Poisson's coefficient of calcite are E_1 = 95 GPa and υ_1 = 0.27, the ones of quartz are E_2 = 101 GPa, υ_2 = 0.06. Given their significantly higher stiffness compared to the clay matrix, the calcite and quartz grains can be collectively regarded as a single family of rigid effective inclusions, with average elastic parameters taken as E^i = 98 GPa and ν^i = 0.15. Accordingly, the claystone is idealized as a composite material featuring a porous matrix-inclusion microstructure, as depicted in Fig. 1. Based on experimental data from [35], the f and ρ at each sampling depth have been quantified. The corresponding test conditions are summarized in Table 1.

Table 1
Values of mineralogical composition and porosity at different depths for the studied composite based on the measurement of [35].

Depths (m)	Confining pressure (MPa)	Inclusion (%)	Clay matrix (%)	Porosity (%)
466.8	0	49	51	23.7
451.5	5	51	49	23.6
451.4	10	53	47	25.0
451.4	20	53	47	25.0
468.9	0	66	34	32.5
469.0	5	56	44	30.5
469.1	10	45	55	20.1
468.9	20	66	34	32.5
482.2	0	40	60	22.9
482.2	5	40	60	22.9
482.2	10	40	60	22.9
482.3	20	55	45	26.2

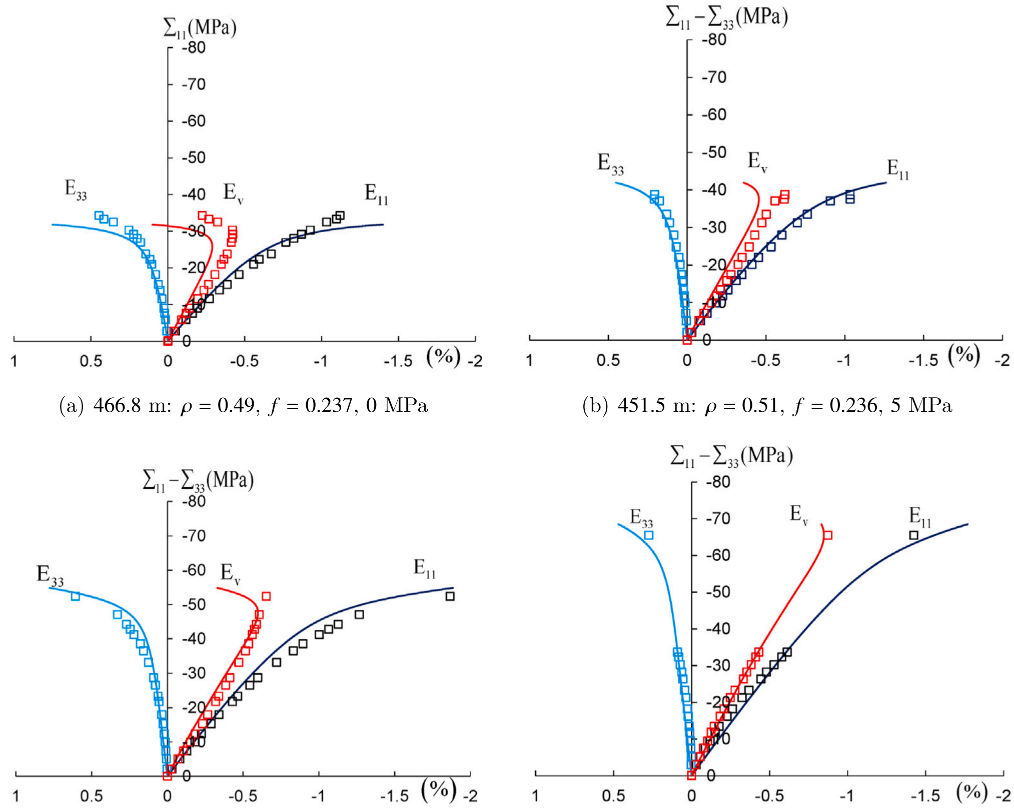

(a) 466.8 m: $\rho = 0.49$, $f = 0.237$, 0 MPa

(b) 451.5 m: $\rho = 0.51$, $f = 0.236$, 5 MPa

(c) 451.4 m: $\rho = 0.53$, $f = 0.25$, 10 MPa

(d) 451.4 m: $\rho = 0.53$, $f = 0.25$, 20 MPa

Fig. 8. Numerical simulation results (solid lines) versus experimental data (symbols) from [35] under confining pressures at depth 1.

4.1. Effective yield surfaces

Based on the compositional data, the strength behavior of the claystone is characterized using the newly developed effective strength criterion given in Eq. (14). Experimental results of yield surfaces at various depths, as reported in [35], are examined here. Figs. 5–7 present the peak strength of the investigated claystone in the Σ_{eq} - Σ_m plane for each depth, under different confining pressures: 0, 5, 10, and 20 MPa. These are represented respectively by asterisk, box, circle, and diamond symbols. The solid curves correspond to the yield surfaces predicted by the proposed macroscopic criterion in Eq. (14). Table 1 summarizes the ρ and f at each depth. For simplicity, the parameter υ^{mp} is fixed at 0.47. The values adopted for the asymptotic frictional coefficient and local hydrostatic tensile strength are $T_m = 0.81$ and $h = 15$ MPa, respectively. Overall, a satisfactory agreement is observed between the experimental data and the predictions from the proposed yield criterion. The model effectively accounts for the influence of confining pressure and key microstructural features, such as porosity and inclusion content, on the overall mechanical response.

The effect of mineral inclusion on the material strength has been investigated in [26] by the Hill's incremental approach and in [16,27,28] by the modified secant method. However, the influence of pore has been neglected in these works. To better understand the effects material microstructure on the overall strength of the studied composite, Fig. 4 illustrates the yield strengths predicted by the novel criterion Eq. (14) with different values of f and ρ, $T = 0.81$ and $h = 15$ MPa. The material reinforced by the increase of the volume fraction of mineral grains and weakened by the increase of porosity.

The next step involves determining the parameters for the constitutive model. Following this, the fully defined model will be employed to simulate the stress–strain relations observed in the claystone.

4.2. Identification of the model's parameters

The elastoplastic constitutive model described in the preceding section involves four elastic parameters that require calibration: the Young's modulus and Poisson's ratio of the effective inclusion (E^i, υ^i), as well as those of the solid phase (E^s, υ^s) at the microscale. As previously established, the values $E^i = 98$ GPa and $\upsilon^i = 0.15$ have been adopted. The elastic characteristics of the solid phase can be derived from the relationships linking the homogenized moduli (μ^{hom}, κ^{hom}) at the macroscale, the moduli of the porous matrix (μ^{mp}, κ^{mp}) at the mesoscale, and the corresponding moduli (μ, κ) of the solid phase at the microscale. The general procedure is given as follows: using the elastic segment of the experimental stress–strain curve, the macroscopic Young's modulus E^{hom} and Poisson's ratio υ^{hom} of the composite can be obtained, which can be changed to the bulk modulus μ^{hom} and shear modulus κ^{hom}. According to the ones of the mineral grains μ^i and κ^i and its volume fraction ρ at the mesoscopic scale, the corresponding μ^{mp} and κ^{mp} of the porous matrix can be calculated by solving the system of two Eqs. (A.1) and (A.2). Substituting these obtained values and also the porosity f into the Eq. (12), one can get directly the bulk and shear moduli μ and κ (or the Young's modulus E^s and Poisson's ratio υ^s) of the solid phase at the microscopic scale. With regard to the plastic parameters, the asymptotic friction coefficient T_m and the local hydrostatic tensile strength h were calibrated in the previous section by

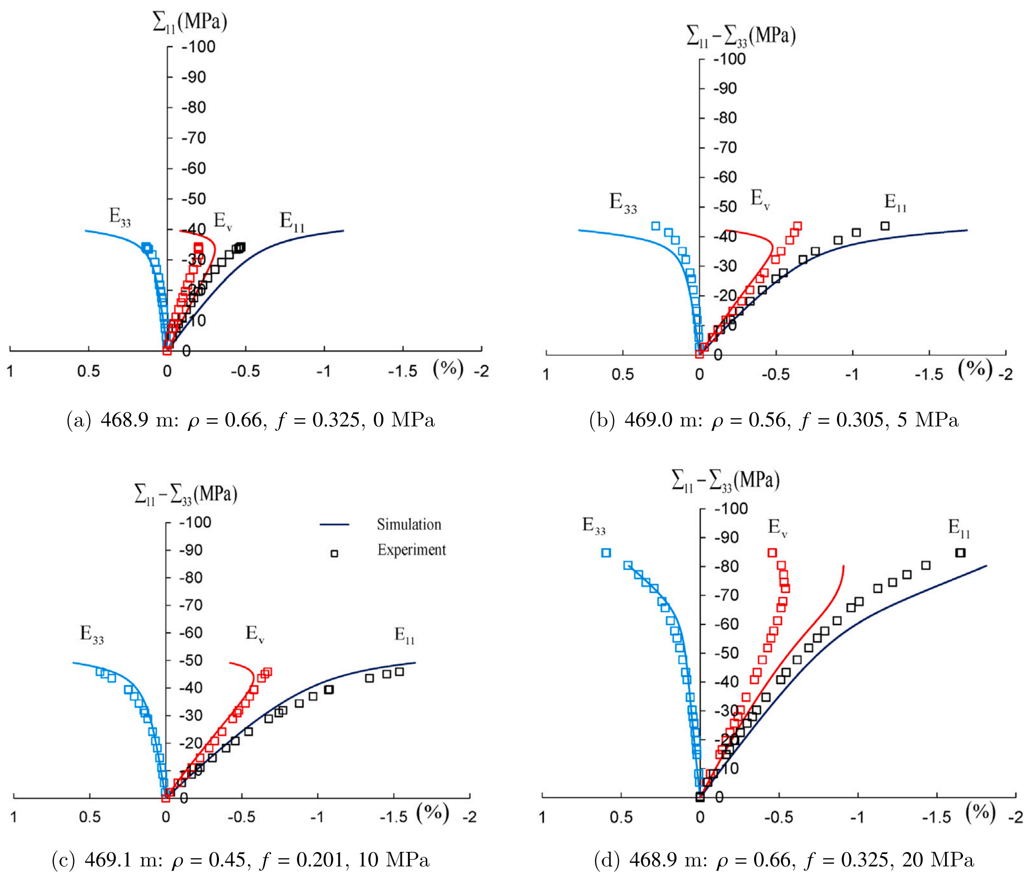

Fig. 9. Numerical simulation results (solid lines) versus experimental data (symbols) from [35] under confining pressures at depth 2.

comparing the experimental yield surfaces with those predicted by the effective strength criterion Eq. (14). The parameter T_0 defines the initial yield threshold, while b_1 governs the hardening evolution. Dilatancy behavior, reflected in macroscopic lateral or volumetric strains, is regulated by the parameters t_0, t_m, and b_2. These values are readily identified through a fitting procedure applied to a representative experimental stress–strain curve. Table 2 summarizes the full set of parameter values adopted in the proposed constitutive model.

Table 2
Model's parameters for the studied claystone.

	Solid phase	Effective grain
Elastic:	$E^s = 3$ GPa, $\upsilon^s = 0.2$	$E^i = 98$ GPa, $\upsilon^i = 0.15$
Plastic:	$T_0 = t_0 = 0.01$, $T_m = 0.81$, $b_1 = 0.0011$, $t_m = 0.67$, $b_2 = 0.005$, $h = 15$ MPa	

4.3. Experimental validation

Following the calibration of elastic and plastic parameters, the developed model will be employed to characterize the macroscopic mechanical response of the studied claystone, accounting for the influence of mineral composition and porosity, as well as their evolution throughout the loading process. To comprehensively evaluate the performance of the constitutive model, a series of uniaxial and triaxial compression simulations are conducted on samples originating from different depths. The simulations incorporate confining pressures of 0, 5, 10, and 20 MPa, consistent with the experimental conditions reported in [35]. All simulations utilize the same parameter set provided in Table 2, while the corresponding ρ and f at each depth are summarized in Table 1. A comparison between numerical predictions (solid lines) and experimental data (points) under various confining pressures is presented in Figs. 8–10, corresponding to three distinct depths. Comparing with the results in Figs. 8–9, the discrepancies between these two results are more noticeable in Fig. 10. This is mainly due to the variability of specimens and the simplification done in this model. According to the material studied, a representative volume element with small pores at the microscopic scale and big inclusions at the mesoscopic scale is adopted. Although we considered the distribution of pores and inclusions at different scales as well as the influence of the solid matrix properties, the real microstructure of this claystone is more complex. For example, the shapes of pores and mineral grains are not spherical; there are some meso-pores in some specimens, and so on. Overall, a close match is observed between the simulations and the experimental results. The proposed model effectively captures key mechanical characteristics of the claystone, including the transition from contractive to dilative behavior with increasing deviatoric stress, as well as the effect of confining pressure on the overall stress–strain response. Furthermore, the macroscopic behavior of the claystone is shown to be significantly influenced by the volume fraction of inclusions ρ and the porosity f. Fig. 11 illustrates the evolution of the inclusion content ρ and porosity f obtained from numerical simulations at depth 1. The proposed micromechanics-based constitutive model effectively captures these microstructural evolution processes during loading. This capability represents a key advantage of micro–macro constitutive models over phenomenological approaches.

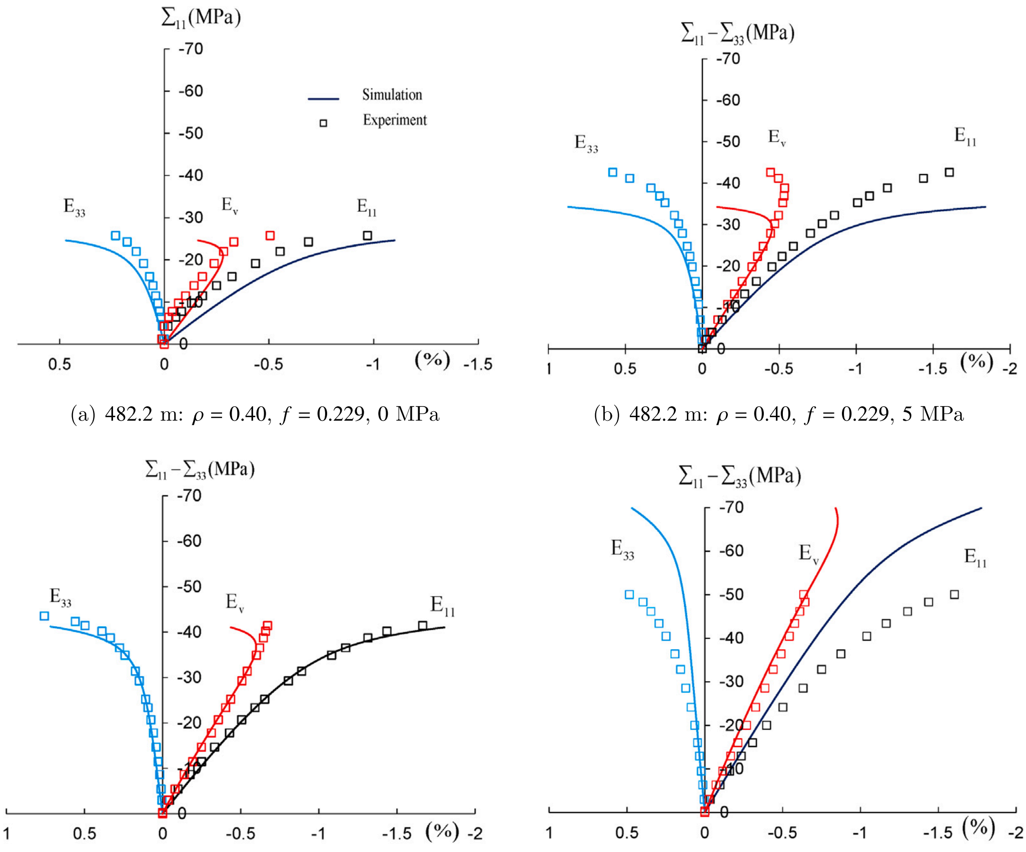

(a) 482.2 m: $\rho = 0.40$, $f = 0.229$, 0 MPa

(b) 482.2 m: $\rho = 0.40$, $f = 0.229$, 5 MPa

(c) 482.2 m: $\rho = 0.40$, $f = 0.229$, 10 MPa

(d) 482.3 m: $\rho = 0.55$, $f = 0.262$, 20 MPa

Fig. 10. Numerical simulation results (solid lines) versus experimental data (symbols) from [35] under confining pressures at depth 3.

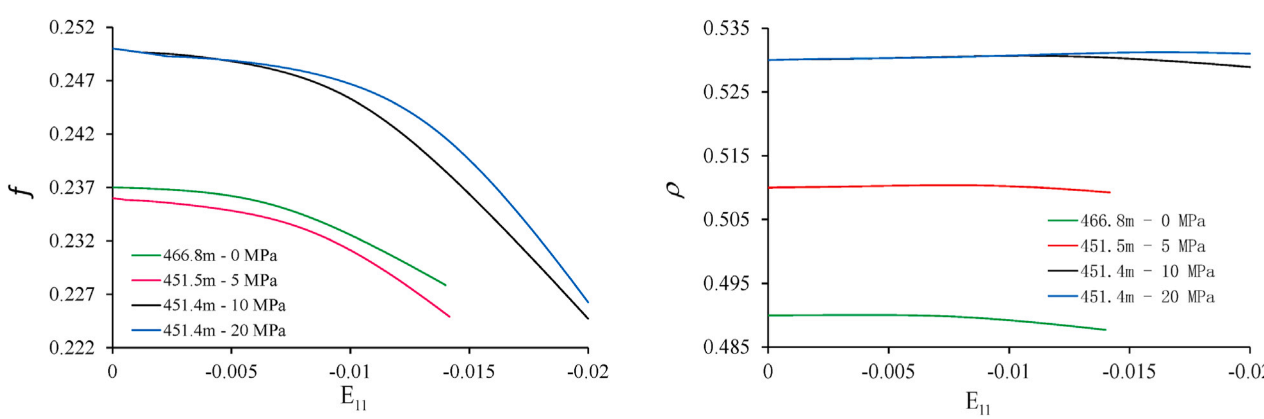

(a) Variation of f

(b) Variation of ρ

Fig. 11. Variations of f and ρ with axial strain under different confining pressures for depth 1 samples.

5. Conclusions

In this study, a novel micromechanics-based constitutive model is developed for heterogeneous materials characterized by a porous matrix-inclusion microstructure. The model builds upon a newly derived effective strength criterion that concurrently incorporates the effects of inclusion volume fraction at the mesoscale and matrix porosity at the microscale, along with the pressure sensitivity of the solid phase. This proposed criterion offers improvements over existing one. A full constitutive description is then established by introducing an appropriate hardening law and a macroscopic plastic potential. Following parameter identification, the multiscale model is applied to characterize the macroscopic mechanical behavior of a typical claystone. The plastic yield surface is first examined. Subsequently, numerical simulations are performed on samples from different depths with different mineral compositions and porosities. The model effectively accounts for microstructural information and its evolution, as demonstrated by favorable comparisons between predictions and experimental data under various confining pressures. The proposed model successfully captures the key mechanical features of the investigated claystone.

CRediT authorship contribution statement

Wanqing Shen: Methodology, Conceptualization, Data curation, Investigation, Writing – original draft, Writing – review & editing, Validation, Visualization.

Declaration of Competing Interest

The author declares that he has no known competing financial interests or personal relationships that could have appeared to influence the work reported in this paper.

Acknowledgments

This study was partially supported by the Programme B18019 of Discipline Expertise to Universities MOE & MST, France.

Appendix. Macroscopic bulk modulus κ^{hom} and shear modulus μ^{hom} given by [31,32]

The effective bulk modulus κ^{hom} of composites reinforced with spherical particles has been studied in [31,32] using the generalized self-consistent method. It is expressed as follows:

$$\kappa^{hom} = \kappa^m - \frac{(3\kappa^m + 4\mu^m)(\kappa^m - \kappa^i)\rho}{(3\kappa^i + 4\mu^m) + 3(\kappa^m - \kappa^i)\rho} \tag{A.1}$$

According to [31,32], the effective shear modulus μ^{hom} is defined by the following Eq. (A.2), which is established on the basis of Eshelby's energy equivalence condition:

$$A\left(\frac{\mu^{hom}}{\mu^m}\right)^2 + B\left(\frac{\mu^{hom}}{\mu^m}\right) + C = 0 \tag{A.2}$$

In this expression, μ^m represents the shear modulus of the matrix material, which is strengthened by the presence of inclusions. The parameters A, B, and C are defined as follows, where μ^i denotes the shear modulus of the inclusion, while ν^i and ν^m correspond to the Poisson's ratios of the inclusion and the matrix, respectively:

$$\begin{aligned}
A = {} & 8\left(\frac{\mu^i}{\mu^m} - 1\right)(4 - 5\nu^m)\eta_1\rho^{10/3} - 2\left[63\left(\frac{\mu^i}{\mu^m} - 1\right)\eta_2 + 2\eta_1\eta_3\right]\rho^{7/3} \\
& +252\left(\frac{\mu^i}{\mu^m} - 1\right)\eta_2\rho^{5/3} - 50\left(\frac{\mu^i}{\mu^m} - 1\right)(7 - 12\nu^m + 8\nu^{m2})\eta_2\rho \\
& +4(7 - 10\nu^m)\eta_2\eta_3 \\
B = {} & -4\left(\frac{\mu^i}{\mu^m} - 1\right)(1 - 5\nu^m)\eta_1\rho^{10/3} + 4\left[63\left(\frac{\mu^i}{\mu^m} - 1\right)\eta_2 + 2\eta_1\eta_3\right]\rho^{7/3} \\
& -504\left(\frac{\mu^i}{\mu^m} - 1\right)\eta_2\rho^{5/3} + 150\left(\frac{\mu^i}{\mu^m} - 1\right)\nu^m(3 - \nu^m)\eta_2\rho \\
& +3(15\nu^m - 7)\eta_2\eta_3 \\
C = {} & -4\left(\frac{\mu^i}{\mu^m} - 1\right)(7 - 5\nu^m)\eta_1\rho^{10/3} - 2\left[63\left(\frac{\mu^i}{\mu^m} - 1\right)\eta_2 + 2\eta_1\eta_3\right]\rho^{7/3} \\
& +252\left(\frac{\mu^i}{\mu^m} - 1\right)\eta_2\rho^{5/3} - 25\left(\frac{\mu^i}{\mu^m} - 1\right)(7 - \nu^{m2})\eta_2\rho - (7 + 5\nu^m)\eta_2\eta_3
\end{aligned} \tag{A.3}$$

in which

$$\begin{aligned}
\eta_1 &= (7 + 5\nu_i)(7 - 10\nu^m)\frac{\mu^i}{\mu^m} - (7 - 10\nu_i)(7 + 5\nu^m) \\
\eta_2 &= 4(7 - 10\nu_i) + (7 + 5\nu_i)\frac{\mu^i}{\mu^m} \\
\eta_3 &= (7 - 5\nu^m) + 2(4 - 5\nu^m)\frac{\mu^i}{\mu^m}
\end{aligned} \tag{A.4}$$

Data availability statement

Data used is from a publicly accessible repository cited in the article. The codes used in this work are available upon request.

References

[1] Z. Qin, R.C. Zhang, W.Z. Mao, et al., A meso-damage-based constitutive model for yellow sandstone under dry-wet cycles, Deep Undergr. Sci. Eng. 3 (4) (2024) 497–507.
[2] D.X. Chen, L.G. Wang, P.D. Versaillot, et al., Triaxial creep damage characteristics of sandstone under high crustal stress and its constitutive model for engineering application, Deep Undergr. Sci. Eng. 2 (3) (2023) 262–273.
[3] G. Zhang, L.K. Xie, Y. Gao, et al., Three-dimensional strength estimation and elastic–plastic constitutive model with double yield surfaces of porous sandstone, Appl. Geophys. 23 (1) (2026) 182–201.
[4] Z.B. Liu, H.S. Oh, M. Wu, et al., Creep behavior of mélange rocks and the hardening-damage nonlinear elastic-viscous model, Pure Appl. Geophys. 182 (2) (2025) 587–608.
[5] C.A. Coulomb, Essai sur une application des regles des maximis et minimis a quelquels problemesde statique relatifs, a la architecture, Mem. Acad. Roy. Div. Sav. 7 (1776) 343–387.
[6] D.C. Drucker, W. Prager, Soil mechanics and plastic analysis or limit design, Quart. Appl. Math. 10 (2) (1952) 157–165.
[7] E. Hoek, E.T. Brown, Empirical strength criterion for rock masses, J. Geotech. Eng. Div. 106 (9) (1980) 1013–1035.
[8] F. Tian, Z.B. Liu, H.B. Li, et al., Advances in peridynamics modeling of deformation and fracturing of brittle geomaterials, Deep Resour. Eng. 1 (3) (2024) 100110.
[9] A.L. Gurson, Continuum theory of ductile rupture by void nucleation and growth: Part 1-yield criteria and flow rules for porous ductile media, J. Eng. Mater. Technol. 99 (1) (1977) 2–15.
[10] W.Q. Shen, Approximate plastic yield criteria of geomaterials with pores and grains embedded in a porous matrix, Int. J. Plast. 153 (2022) 103275.
[11] J.H. Lee, J. Oung, Yield functions and flow rules for porous pressure-dependent strain-hardening polymeric materials, J. Appl. Mech. 67 (2) (2000) 288–297.
[12] H.Y. Jeong, A new yield function and a hydrostatic stress-controlled void nucleation model for porous solids with pressure-sensitive matrices, Int. J. Solids Struct. 39 (5) (2002) 1385–1403.
[13] T.F. Guo, J. Faleskog, C.F. Shih, Continuum modeling of a porous solid with pressure sensitive dilatant matrix, J. Mech. Phys. Solids 56 (6) (2008) 2188–2212.
[14] M. Trillat, J. Pastor, Limit analysis and Gurson's model, Eur. J. Mech. A/Solids 24 (5) (2005) 800–819.
[15] W.Q. Shen, A micromechanics-based multiscale constitutive model for brittle to ductile behavior of porous geomaterial, Rock Mech. Rock Eng. 57 (2024) 7205–7221.
[16] S. Maghous, L. Dormieux, J.F. Barthélémy, Micromechanical approach to the strength properties of frictional geomaterials, Eur. J. Mech. A/Solids 28 (1) (2009) 179–188.
[17] J-F. Barthelemy, L. Dormieux, Détermination du critère de rupture macroscopique d'un milieu poreux par homogénéisation non linéaire, C. R. Mec. 331 (4) (2003) 271–276.
[18] J.Q. Yu, Y. Wu, J.M. Wang, et al., Analysis of physico-mechanical properties and pore structure characteristics of thermally damaged sandstone, Deep Resour. Eng. 2 (4) (2025) 100188.
[19] T. Meng, Z.B. Liu, F.B. Wu, et al., Coupled thermo-hydro-mechanical analysis of porous rocks: Candidate of surrounding rocks for deep geological repositories, J. Rock Mech. Geotech. Eng. 17 (5) (2025) 3073–3092.
[20] K. Ng, J.C. Santamarina, Mechanical and hydraulic properties of carbonate rock: The critical role of porosity, J. Rock Mech. Geotech. Eng. 15 (4) (2023) 814–825.
[21] X.T. Feng, C.X. Yang, B.G. He, et al., Artificial intelligence technology in rock mechanics and rock engineering, Deep Resour. Eng. 1 (2) (2024) 100008.
[22] M. Hussain, U. Shakir, Z. Naseer, et al., Integrating conventional and machine learning approaches with seismic inversion for optimized porosity estimation in heterogeneous siliciclastic rocks, Phys. Chem. Earth, Parts A/B/C 142 (2026) 104248.
[23] Andra, Referentiel du site Meuse-Haute Marne, Report No. C.RP.ADS.04.0022, Paris, France (2005) https://international.andra.fr.
[24] H. Wang, X.Q. Xu, Z.F. Wu, et al., A study on the safety of nuclear waste isolation in claystone under coupled hydro-mechanical-seepage processes: An engineering geology perspective based on a generalized numerical model, Deep Resour. Eng. (2025) 100234.
[25] J.C. Robinet, Mineralogie, porosite et diffusion des solutes dans l'argilite du Callovo-Oxfordien de Bure (Meuse/Haute-Marne, France) de l'echelle centimetrique a micrometrique, PhD Thesis, Université de Poitiers, France, 2008.
[26] A. Abou-Chakra Guéry, F. Cormery, J.F. Shao, et al., A micromechanical model of elastoplastic and damage behavior of a cohesive geomaterial, Int. J. Solids Struct. 45 (5) (2008) 1406–1429.

[27] J.F. Barthélémy, L. Dormieux, A micromechanical approach to the strength criterion of Drucker–Prager materials reinforced by rigid inclusions, Int. J. Numer. Anal. Methods Geomech. 28 (7–8) (2004) 565–582.
[28] L. Dormieux, J.F. Barthélémy, S. Maghous, Résistance d'un composite à renforts rigides : Le cas d'une matrice de Drucker–Prager avec règle d'écoulement plastique non associée, C. R. Mec. 334 (2) (2006) 111–116.
[29] C. Zhang, S. Jia, Z.P. Ren, et al., Strength evolution characteristics of coal with different pore structures and mineral inclusions based on CT scanning reconstruction, Nat. Resour. Res. 33 (6) (2024) 2725–2742.
[30] W.Q. Shen, Y.J. Cao, J.L. Chen, et al., The influence of mineral inclusion on the effective strength of rock-like geomaterials, Int. J. Plast. 181 (2024) 104104.
[31] Z.X. Lu, The effective moduli of composite reinforced by spherical coating particles, Appl. Math. Mech. 19 (10) (1998) 997–1006.
[32] R.M. Christensen, K.H. Lo, Solutions for effective shear properties in three phase sphere and cylinder models, J. Mech. Phys. Solids 27 (4) (1979) 315–330.
[33] H.Y. Jeong, J. Pan, A macroscopic constitutive law for porous solids with pressure-sensitive matrices and its implications to plastic flow localization, Int. J. Solids Struct. 32 (24) (1995) 3669–3691.
[34] W.Q. Shen, J.F. Shao, Z.B. Liu, et al., Evaluation and improvement of macroscopic yield criteria of porous media having a Drucker–Prager matrix, Int. J. Plast. 126 (2020) 102609.
[35] A.S. Chiarelli, J.F. Shao, N. Hoteit, Modeling of elastoplastic damage behavior of a claystone, Int. J. Plast. 19 (1) (2003) 23–45.
[36] T. Mori, K. Tanaka, Average stress in matrix and average elastic energy of materials with misfitting inclusions, Acta Metall. 21 (5) (1973) 571–574.
[37] W.Q. Shen, A new yield criterion based constitutive model for porous materials, Int. J. Mech. Sci. 274 (2024) 109250.
[38] W.Q. Shen, The influences of temperature on the macroscopic elastoplastic behaviors of heterogeneous materials, Mech. Mater. 199 (2024) 105176.
[39] A.S. Chiarelli, Etude expérimentale et modélisation du comportement mécanique de l'argilite de l'Est: Influence de la profondeur et de la teneur en eau, PhD Thesis, Université de Lille, France, 2000.

Dr. Wanqing Shen is currently an Associate Professor at the University of Lille, France. He investigates the relationship between the microstructures and the macroscopic mechanical behaviors of heterogeneous materials by theoretical and numerical methods, also the applications of artificial intelligence in geomaterials. A series of original micromechanics-based multiscale models has been constructed and widely applied to various engineering fields such as petroleum industry, geological disposal of nuclear waste. He is the author and co-author of 95 papers in peer-reviewed SCI journal papers, including 5 articles as sole author. He obtained the Prize of Excellent Scientific Research and Supervision (Prime d'Encadrement Doctoral et de Recherche) in 2017 and 2021, which is evaluated by the National Council of Universities (CNU) of France and the Chinese Government Award For Outstanding Self-Financed Students Abroad in 2011.